entropy

MDPI

Article

Universality and beyond in Optical Microcavity Billiards with Source-Induced Dynamics

Lukas Seemann and Martina Hentschel *

Institute of Physics, Technische Universität Chemnitz, D-09107 Chemnitz, Germany
* Correspondence: martina.hentschel@physik.tu-chemnitz.de

Abstract: Optical microcavity billiards are a paradigm of a mesoscopic model system for quantum chaos. We demonstrate the action and origin of ray-wave correspondence in real and phase space using far-field emission characteristics and Husimi functions. Whereas universality induced by the invariant-measure dominated far-field emission is known to be a feature shaping the properties of many lasing optical microcavities, the situation changes in the presence of sources that we discuss here. We investigate the source-induced dynamics and the resulting limits of universality while we find ray-picture results to remain a useful tool in order to understand the wave behaviour of optical microcavities with sources. We demonstrate the source-induced dynamics in phase space from the source ignition until a stationary regime is reached comparing results from ray, ray-with-phase, and wave simulations and explore ray–wave correspondence.

Keywords: microcavity billiards; sources; ray–wave correspondence; phase-space dynamics; Husimi function; quantum chaos

Citation: Seemann, L.; Hentschel, M. Universality and beyond in Optical Microcavity Billiards with Source-Induced Dynamics. *Entropy* **2023**, *25*, 95. https://doi.org/10.3390/e25010095

Academic Editor: Marko Robnik

Received: 10 December 2022
Revised: 22 December 2022
Accepted: 29 December 2022
Published: 3 January 2023

1. Introduction

Two-dimensional (2D) systems have inspired the field of quantum chaos for many years [1–3]. The origins of studying the quantum mechanical pendants of classically non-integrable systems trace back to the 1980s when universality was established as a common property of very different chaotic systems [4,5], in particular in the energy-level statistics in the 1980 paper of Casati et al. [4], and a variety of studies have been initiated focusing on the statistical properties based, e.g., on Random Matrix Theory [6].

The impressive properties of this new class of mesoscopic model systems [7] for both electrons and photons soon initiated interest in possible applications. Besides the ballistic quantum dots [3], the optical microcavities [8–14] have received a lot of interest, and lately also in non-euclidean [15] and Dirac Fermion optics [16]. One practical motivation was certainly the realization of microcavity lasers with directional emission, and plenty of solutions were found and investigated [17]. One realization involves deformed microdisk cavities of various shapes [18], including the Limaçon cavity [19–25]. Besides the experimental verification of the predicted [19] directional and universal, resonance-independent far-field emission originating from the cavity's invariant manifold, a remarkable ray–wave correspondence was seen. While all results were obtained for very different wavelengths λ—the ray modeling in the $\lambda \to 0$-limit, the wave simulation for λ larger than the experimentally relevant values—the agreement between all three approaches was convincing with slight, interference-inspired deviations between the three curves. Shinohara et al. [22] complemented this interpretation nicely by showing that averaging over a large number of resonances (42 in Ref. [22]) improves ray–wave correspondence by averaging out the resonance-specific features.

The reason for the universality of the observed far-field emission properties of whispering-gallery (WG)-type modes with high Q-factors is that the so-called natural measure (or Fresnel-weighted unstable manifold or steady probability distribution) [26]

determines the emission characteristics. Assuming a light ray to be initially captured by total internal reflection, it will, in a chaotic cavity, undergo a number of reflections where this condition remains fulfilled. However, at one point it will be violated and the angle of incidence χ will cross the critical lines $\sin \chi_c = \pm 1/n$ in phase space (n is refractive index of the cavity and we assume $n_0 = 1$ outside), and ray splitting occurs with the amount of light remaining in the cavity determined by Fresnel's reflection coefficient. The crossing of the critical line will be ruled by the unstable manifold of the system, weighted by the Fresnel reflection coefficient for our open optical system. Notice that this quantity describes the expanding directions along which the light will escape the cavity (actually, in the wave picture, by evanescent or tunneling escape from high-Q modes). This implies that the unstable manifold, as an important and central, yet abstract quantity of nonlinear dynamics is directly accessible and visible in experiments and the corresponding simulations. We point out that, therefore, simulations of the passive, non-lasing cavity can successfully describe even lasing cavities as long as mode interactions [27] do not play a role. In terms of ray picture modeling, the initial conditions are homogeneously distributed in phase space and the far-field characteristics are recorded when an initial transient regime is lapsed.

In this paper, we will explore another situation in optical microcavities that is induced by the presence of sources (or, similarly, relevant in microlasers with non-uniform pumping conditions [28,29]). This setting can capture situations where not all initial conditions are homogeneously populated, in contrast to the microlaser case discussed above. Source-induced phenomena can be relevant, for example, due to a specific distribution of fluorescent particles, a local pumping scheme, or even due to the coupling of two or more systems that effectively change the initial conditions to be non-uniform in phase space. The base element of any source can be described as a point-like emitter.

The paper is organized as follows. We will consider point-like sources and study their impact on the far-field emission in Section 2. We then investigate the source-initiated dynamics in phase space and introduce a ray picture extended by the phase information in Section 3 before we end with a conclusion and summary in Section 4.

2. Optical Microcavity Billiards with Sources

We start our investigation for a Limaçon cavity [19] with the shape given in polar coordinates (r, ϕ) as $r(\phi) = R_0(1 + \epsilon \cos \phi)$ where we set $R_0 = 1$ and choose the deformation parameter $\epsilon = 0.43$, such that the phase space of the cavity is known to be almost fully chaotic. We use Birkhoff coordinates, i.e., the arclength s along the boundary starting at its intersection with the positive x axis, and the sine of the angle of incidence χ of light traveling inside the cavity to specify the position in phase space. The far-field angle φ_{ff} is measured to be mathematically positive with respect to the positive x axis. We will consider TM polarized light (electric field transverse to the resonator plane, i.e. along the z axis, $\vec{E} = E_z \vec{e_z}$), a refractive index $n = 3.3$, and vary the position x_s of the source along the x axis. We use simulations with the open-source software package meep [30] and so-called meep units with the velocity of light set to 1, such that frequency f and (vacuum) wavelength λ are reciprocal to each other, as is the period $T = 1/f$. We use the built-in continuous source function of meep to describe a point-like coherent source that oscillates as $\exp(-2\pi i f t)$. Such a point-like source can be considered the basic module of any other source distribution.

Variation of the source position. For a mode at resonance frequency $f = 1.2$ (corresponding to $nkR \approx 25$), the far-field emission depends critically on the source position x_s as is visible in Figure 1. In general, more central source positions relate to more isotropic emissions, and the far-field emission characteristics of the uniformly pumped cavity can be completely lost. Similar results were found in a study of graphene and optical billiards in Ref. [16], where the importance of lensing effects in particular for single-layer graphene cavities was discussed.

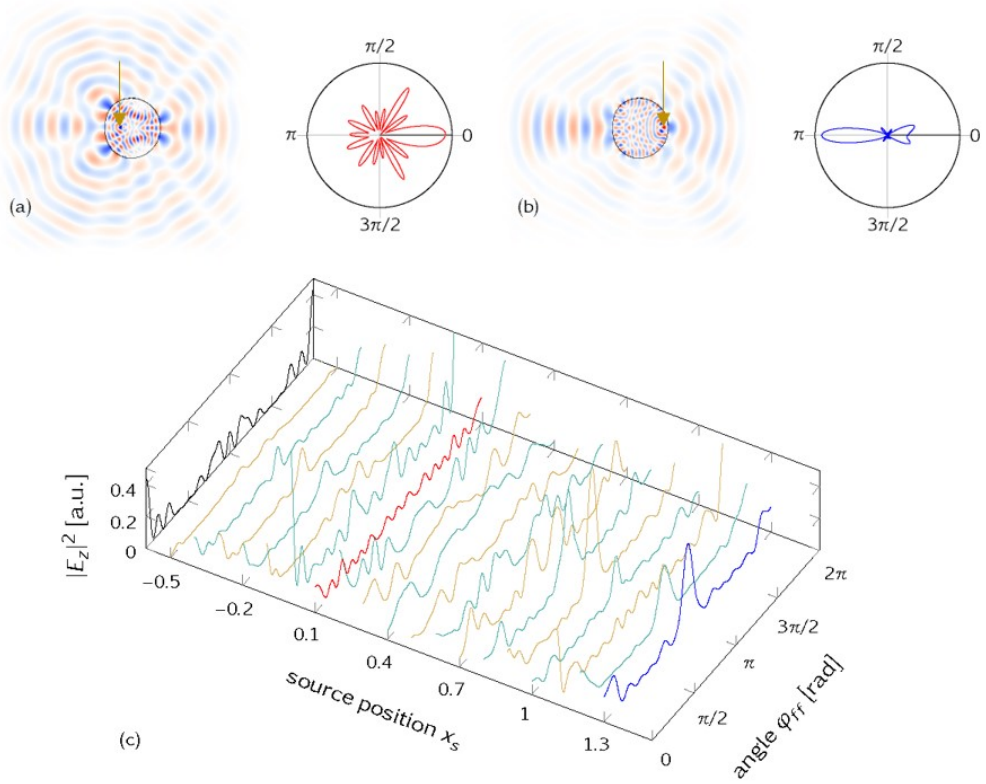

Figure 1. (**a**) Amplitude distribution E_z in real space for a mode at resonant frequency $f = 1.2$ and source position $x_s = 0.1$ (marked by arrow), and corresponding far-field emission as polar plot φ_{ff}. (**b**) Same for $x_s = 1.3$. (**c**) Far-field emission $|E_z|^2$ for source positions x_s varied along the x-axis, revealing a high sensitivity on x_s. The black line on the left marks the far-field emission "without source", i.e., the initial conditions uniformly distributed in phase space, and far-field data are taken when a stationary regime with exponential total internal intensity decay was reached, i.e., omitting the contribution of short rays.

Despite this deviation from the universality seen in the uniform pumping case, ray–wave correspondence still holds as illustrated in Figure 2 for $x_s = 1.3$. The far-field wave intensity $I = |E_z|^2$ and the ray-simulated intensities agree reasonably well. In particular, we find the wave intensity I to be reproduced by the short rays with trajectory lengths $l < 3$ corresponding to typically very few reflections at the system boundary. In other words, in the presence of sources, the far field is mainly determined by refractive escape of rays leaving the source and dwelling of very few reflections in the cavity. This indicates the relevance of lensing effects when the cavity acts similar to a thick lens. However, longer rays are needed to establish a semiquantitative agreement with the wave result for all far-field angles φ_{ff}. These long trajectories carry the information of the cavity geometry as a whole, namely in terms of the unstable manifold.

Variation of the source frequency. It is worthwhile to characterize the far-field sensitivity against variations in the source frequency, cf. Figure 3. In Figure 3a,b, mode patterns (amplitude E_z) are shown for two different frequencies f: resonant ($f = 1.2$) in Figure 3a and off-resonant ($f = 1.6$) in Figure 3b. The source position is fixed again on the x axis, here at $x_s = -0.42$ (marked by arrows). While the intra-cavity patterns deviate a lot—as expected upon a change in wavelength—the emission characteristics are less affected, cf. Figure 3c.

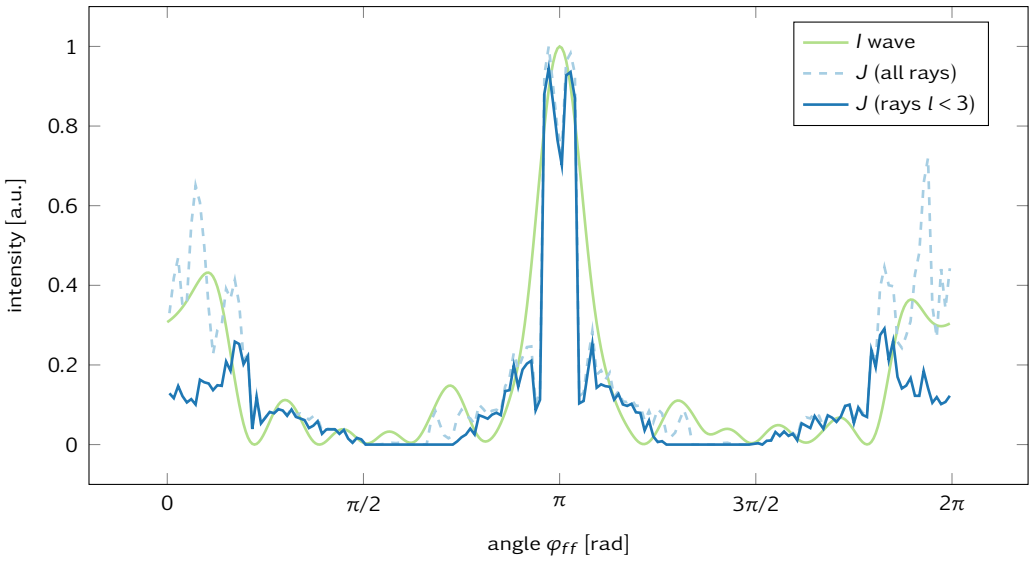

Figure 2. Far-field emission for source position $x_s = 1.3$. Wave intensity $I = |E_z|^2$ for the resonance at frequency $f = 1.2$ (full green line) and for ray-simulated intensities J including the far-field contribution of short rays only (full blue line) and of all rays (dashed line). Evidently, short rays with a trajectory length $l < 3$ contribute significantly to the far-field emission.

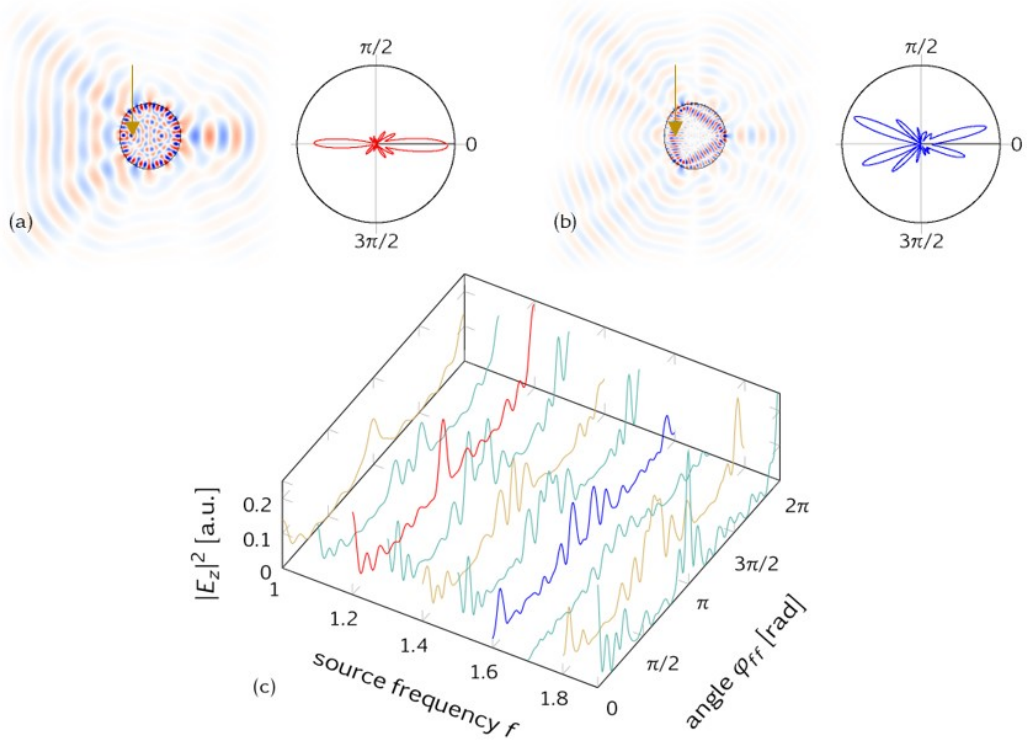

Figure 3. Far field emission depending on the source frequency f, while the source position is fixed at $x_s = -0.42$ (marked by arrow). (**a**) At the resonance frequency $f = 1.2$, the real space amplitude E_z and the far-field emission (polar plot) are shown. (**b**) An off-resonant frequency $f = 1.6$ yields a different mode pattern and a far field that differs in the details, but preserves the generic emission characteristics towards $\varphi_{ff} = 0$ and π. (**c**) Comparison of different source frequencies f confirms that the details are frequency-dependent, while the overall far-field emission is rather robust and dominated by the position of the source.

This result may seem surprising at first glance. However, it can be straightforwardly interpreted on the basis of ray-wave correspondence. Our starting point is the ray–wave correspondence for resonant frequencies, as illustrated in Figure 2 and confirmed in numerous other situations. As the naive ray picture does not know about frequencies or wavelengths, this would suggest no frequency dependence of the far-field emission at all. Of course, this cannot be correct as we know that the details of the far-field emission will be resonance-, or more generally, frequency-dependent [22]. This is precisely what can be seen in Figure 3c. This interpretation is also consistent with the fact that the far-field patterns are determined by short ray trajectories, i.e., before the formation of resonances can be expected.

3. Source-Induced Dynamics: Ray–Wave Correspondence in Phase Space

So far, we have discussed the implications of the presence of sources inside billiards for light, mainly in real space and in terms of far fields, and for the stationary situation. We will now complement the discussion in phase space, discussing both the Husimi function [31] and the ray signature of the source-induced dynamics. To this end, we will discuss the dynamics initiated when a source is turned on and follow it until a stationary state (with the source constantly emitting) is reached.

We will consider a Limaçon-shaped cavity with an intermediate deformation parameter $\epsilon = 0.25$ where a rich, mixed-phase space is present [32,33] (see the gray structure in Figure 4a). We will compare two source positions on the x axis, namely a rather central position $x_s = 0.6$ and an outer position $x_s = 1.0$, thereby manipulating the excitability of WG-type modes and trajectories. We choose a source frequency of $f = 0.64$ and use meep units as before, such that the period of the oscillation $T = 1/f \approx 1.56$. We will consider 80 time steps per period T and use the time frame number t as our variable of time. The time to travel across the cavity, i.e., to travel the optical distance $2nR_0$, is found to be 6.6 in meep units, so it will take about 4.23 T or approximately $t = 338$ frames (time steps) to travel the cavity's diameter.

Initial dynamics. What is the signature of the light emitted from the source? We start our study in the wave picture and excite a source placed at $x_s = 0.6$ with a (resonant) frequency of $f = 0.64$, cf. Figure 5. The real space evolution of the electromagnetic field amplitude E_z is shown in Figure 5a for $t = 186$, just before emitted light from the source reaches the far cavity interface. The corresponding phase–space representation is shown in Figure 5b, and we use the incoming Husimi function H^1_{in} inside the cavity [31] to characterize its signature at the interface boundary where we will also take the Poincaré surface of the section. We see that H^1_{in} contains the signature of light that has reached the cavity boundary at and around $s \approx 0$.

The snapshots in Figure 5c,d are taken about one period T later when all light emitted from the cavity at $t = 0$ has reached the boundary. There is a distinct extra signature that must characterize light emitted from the source at its first reflection at the cavity interface where the Husimi function H^1_{in} is recorded (see also the yellow line in Figure 4a and the discussion there).

This signature is discussed in more detail in Figure 6 for two different source positions and in the wave- and phase-information extended ray picture, respectively. In addition to the naive ray model considered before, we now include the ray's phase ϕ_p. This phase changes along the trajectory path according to $\phi_p = 2\pi l/\lambda$, with l denoting the optical trajectory length traveled. Upon the reflection at the boundary, an additional phase shift would have to be taken into account; however, we will limit our study to just the time before the first reflection. Note that the wavelength enters the ray picture via the phase, and thus resonance-specific properties can, in principle, become accessible within the ray model.

The Husimi functions shown in Figure 6a,b show comparable signatures and reach higher $|\sin\chi|$ for the outer source position $x_s = 1.0$ in (c) as a direct geometrical consequence of x_s being placed closer to the boundary. Notice that from frame to frame t, the location of the intensity maxima varies somewhat (not shown), indicating the importance

of interference effects. This is straightforwardly confirmed qualitatively in Figure 6c,d where the phase-modulated ray intensity is shown at the first reflection point (in agreement with the time frames chosen for the Husimi plots) and clearly seen to possess a rather similar structure.

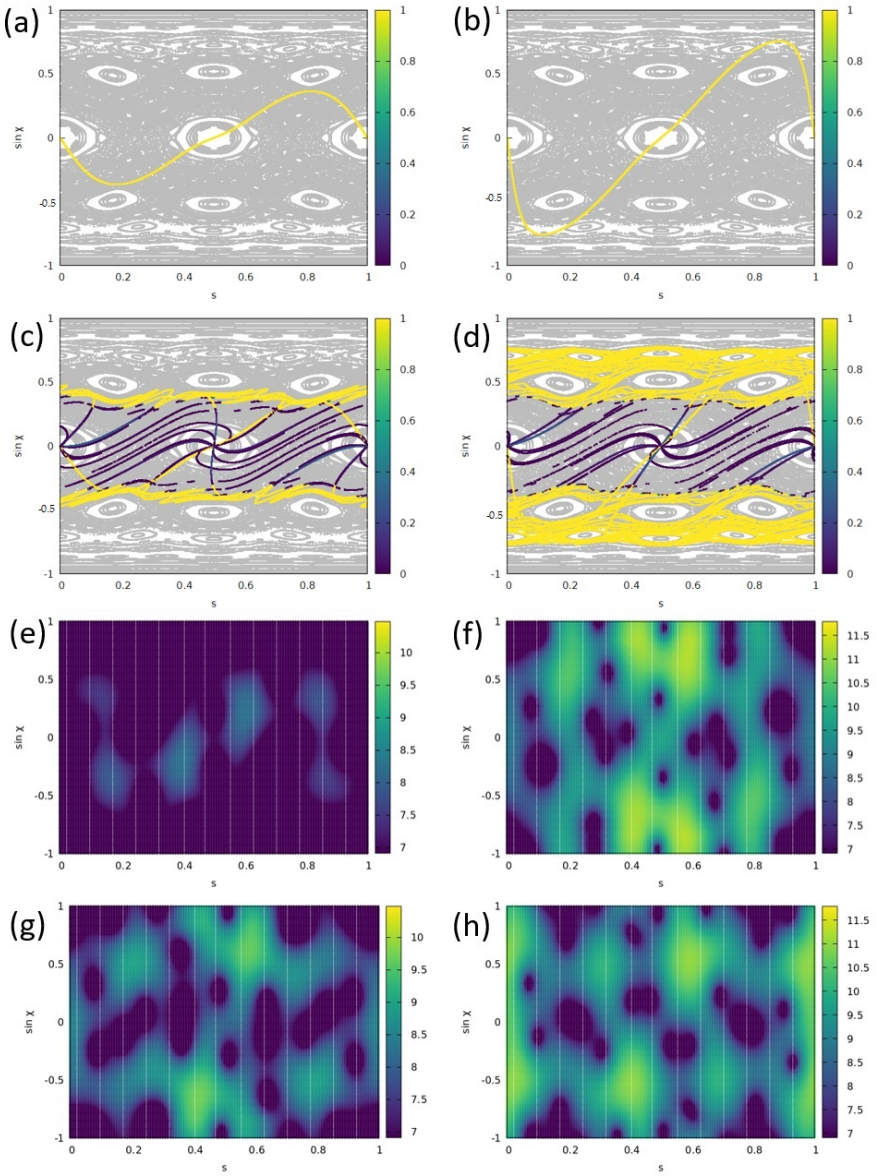

Figure 4. Dynamics induced by the source represented in phase space for two different source positions $x_s = 0.6$ in (**a**,**c**,**e**,**g**) and $x_s = 1$ in (**b**,**d**,**f**,**h**). In the ray simulation results (**a**–**d**), the Poincaré surface of section for a Limaçon cavity with $\epsilon = 0.25$ is indicated as gray background. (**a**,**b**) Characteristiics of a homogeneously emitting source at the first boundary reflection. Shown is the Fresnel-weighted intensity inside the cavity. (**c**,**d**) Same as (**a**,**b**) but after 30 reflections when stationarity is reached. In (**e**–**h**), the wave-simulation results are visualized in phase space in terms of the Husimi function H_{in}^1 when a stationary regime was reached. The Husimi patterns are evolving periodically with period approximately $T/2$, and typical patterns are shown at time frames (**e**) $t = 16$, (**f**) $t = 9$, (**g**) $t = 37$, and (**h**) $t = 30$.

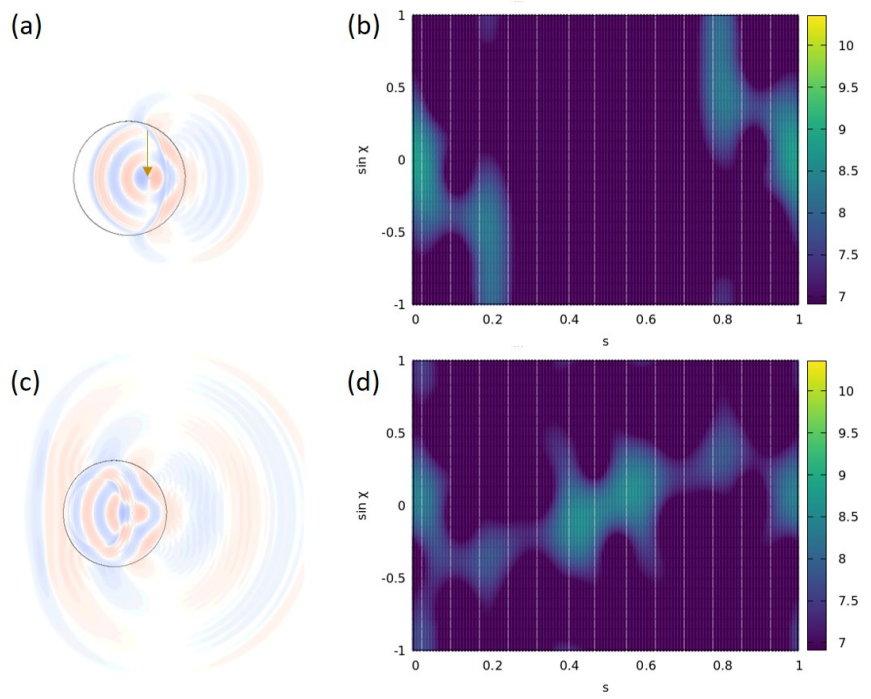

Figure 5. Initial temporal evolution of an electromagnetic wave emitted from a source with $f = 0.64$ at $x_s = 0.6$ (marked by arrow in (**a**)), $\epsilon = 0.25$. (**a**) Real-space E_z and (**b**) phase–space portrait in terms of the Husimi function H^1_{in} at time frame $t = 186$, and similarly one period later at $t = 272$ in (**c**,**d**). Note the extra signature in the center of (**d**) that can be attributed to the source signature after the first reflection at the boundary.

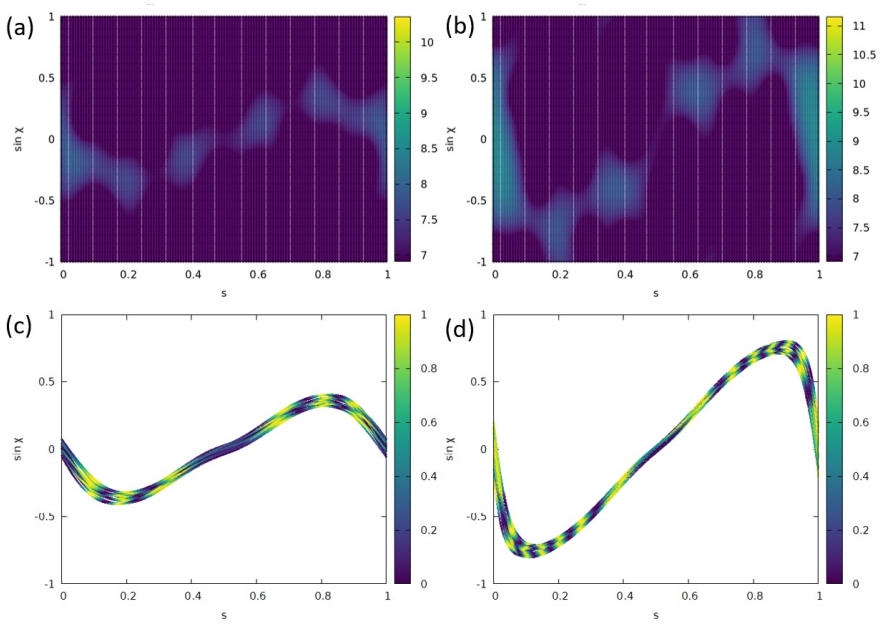

Figure 6. Phase–space representation of light emitted from a source in (**a**,**b**) wave and (**c**,**d**) ray simulations where the ray picture is extended by the phase information. (**a**) Husimi function H^1_{in} for $x_s = 0.6$ and $t = 253$. (**b**) H^1_{in} for $x_s = 1.0$ and $t = 314$. (**c**) Ray-with-phase simulation of the intensity at the first reflection point, 20 sources were randomly placed in a square with side length 0.05 around $x_s = 0.6$ and 2500 rays were started isotropically from each source. (**d**) Same as (**c**) for $x_s = 1.0$.

Stationary dynamics. After having discussed the initial source dynamics, we will now consider the stationary state reached after the transient regime. The results are presented

in Figure 4, again for the source positions $x_s = 0.6$ (left column) and for $x_s = 1.0$ (right column). We start our considerations in the naive ray picture (without phase information) for which we revisit the initial source dynamics in Figure 4a,b. To this end, 10,000 rays are started uniformly from the point-like source and traced to the first reflection with the boundary, yielding the yellow curves. We point out that the time needed for the first reflection point will depend on the starting direction of the ray, especially for non-central x_s. Although the reflection-number based Poincaré map representation will thus differ from the time frame t-based study used in the wave simulations, it still provides a useful tool that can be directly superimposed on the Poincaré surface of section (PSOS). The mixed structure of the PSOS is indicated as the gray background in Figure 4a–d.

In Figure 4c,d, the source has been followed over several reflections at the boundary until stationarity (i.e., intensity saturation) was reached. The phase–space distribution of the Fresnel-weighted intensity emitted by the source is indicated in color scale. The area between the critical lines $\sin\chi = \pm 1/n$ carries a lower intensity due to refractive escape. It is evident that the spread in the phase space depends on the source position—the closer to the boundary x_s is, the larger $|\sin\chi|$ can be reached. In addition, we see that with the source positions chosen here, the three-island orbits cannot be excited within a ray simulation.

The results of wave simulations in the stationary regime (after 50 T) are displayed in Figure 4e–h. For both x_s, we find the pattern of the Husimi function H^1_{in} to periodically (with about $T/2$) vary. For each of the evolutions, we pick two characteristic patterns. For $x_s = 0.6$, we find a typical pattern that represents the source characteristics, cf. Figure 4e. Another one, cf. Figure 4g, displays intensity structured by the three-island chains. Although these islands cannot be populated in the ray-based counterpart model, it may well be possible within wave simulations due to a finite wavelength and when taking semiclassical corrections to the ray picture into account [34–41].

In particular, semiclassical arguments can explain why the intensity maxima in the Husimi function H^1_{in} seem to be placed at somewhat larger $|\sin\chi|$ in comparison to the ray model expectation. In the wave description, the evanescent wave associated with a WG-type mode will penetrate a distance of the order λ into the outer space. The corrected ray picture analogue deploys the Goos–Hänchen shift that causes the reflection to take place at an effective interface [42,43] such that the cavity appears effectively larger. However, then, the Husimi function is determined at a radius R_0 that is too small, thereby making the associated angle of incidence (somewhat) too large, as illustrated in Ref. [36], and thus explaining the deviation.

Eventually, for the other source position $x_s = 1$, we illustrate two typical Husimi patterns in Figure 4f,h. It is evident that now the H^1_{in} reaches larger values $|\sin\chi|$, in agreement with the ray-model expectation. One may speculate about the population of the four-island orbit in Figure 4f or a mode beating interaction induced by the source. We will investigate this in further studies.

4. Conclusions

We have investigated optical microcavities in the presence of sources and discussed and explained source-related (non-)universalities in the ray and wave pictures, and on the grounds of ray–wave correspondence. We showed that the position of a localized source crucially influences the properties of the optical microcavity in comparison to the source-free or uniform situation. These findings can be useful in the context of non-uniformly pumped microlasers or when light is coupled into an optical microcavity at certain positions, for example along the boundary.

We found a good agreement between the ray and wave picture results in terms of far fields and phase–space representations, and identified the signatures of the source in the ray and wave dynamics. We illustrated that a ray picture extended by the phase information can improve the agreement by capturing interference effects and introducing a wavelength into the ray picture. The phase information can also be used to distinguish regular and

chaotic orbits as presented in Figure 7: a chaotic trajectory can be associated with an unpredictable phase value at the reflection points, whereas the phase evolves regularly for a periodic orbit. However, possible source-induced mode (interaction) dynamics [27] that might be suggested by Figure 4 in the stationary regime is beyond the scope of ray–wave correspondence.

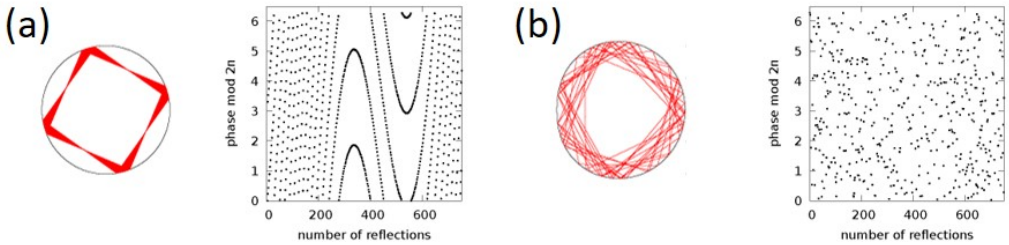

Figure 7. Phase evolution in a ray picture with phase information taken into account for (**a**) a regular orbit ($\epsilon = 0.25$) and (**b**) a chaotic trajectory ($\epsilon = 0.43$).

Author Contributions: Conceptualization, M.H.; Software, L.S.; Investigation, L.S.; Data curation, M.H.; Writing—original draft, M.H.; Visualization, L.S.; Supervision, M.H. All authors have read and agreed to the published version of the manuscript.

Funding: The publication of this article was funded by Chemnitz University of Technology and by the Deutsche Forschungsgemeinschaft (DFG, German Research Foundation)—491193532.

Institutional Review Board Statement: Not applicable.

Data Availability Statement: The data that support the findings of this study are available upon reasonable request from the authors.

Acknowledgments: We thank Tom Rodemund and Marika Carmen Federer for discussions. The special thanks of M.H. goes to Giulio Casati, whom she had the chance to meet several times as a young PhD student when the very basics of this work were laid.

Conflicts of Interest: There is no conflict of interest.

References

1. Stöckmann, H.J. *Quantum Dots: An Introduction*; Cambridge University Press: Cambridge, MA, USA, 1999.
2. Haake, F. *Quantum Signatures of Chaos*; Springer Series in Synergetics; Springer: Berlin, Germany, 2001.
3. Nakamura, K.; Harayama, T. *Quantum Chaos and Quantum Dots*; Oxford University Press: Oxford, UK, 2004.
4. Casati, G.; Val-Gris, F.; Guarnieri, I. On the connection between quantization of nonintegrable systems and statistical theory of spectra. *Lett. Nuovo C. (1971–1985)* **1980**, *28*, 279–282. [CrossRef]
5. Bohigas, O.; Giannoni, M.J.; Schmit, C. Characterization of Chaotic Quantum Spectra and Universality of Level Fluctuation Laws. *Phys. Rev. Lett.* **1984**, *52*, 1–4. [CrossRef]
6. Mehta, M.L. *Random Matrix Theory*; Elsevier: Amsterdam, The Netherlands, 2004.
7. Imry, Y. *Introduction to Mesoscopic Physics*; Oxford University Press: Oxford, UK, 1997.
8. Vahala, K. *Optical Microcavities*; World Scientific: Singapore, 2004.
9. Nöckel, J.U.; Stone, A.D. Ray and wave chaos in asymmetric resonant optical cavities. *Nature* **1997**, *385*, 45–47. [CrossRef]
10. Gmachl, C.; Capasso, F.; Narimanov, E.E.; Nöckel, J.U.; Stone, A.D.; Faist, J.; Sivco, D.L.; Cho, A.Y. High-Power Directional Emission from Microlasers with Chaotic Resonators. *Science* **1998**, *280*, 1556–1564. [CrossRef] [PubMed]
11. Doya, V.; Legrand, O.; Mortessagne, F.; Miniatura, C. Light scarring in an optical fiber. *Phys. Rev. Lett.* **2001**, *88*, 014102. [CrossRef]
12. Schäfer, R.; Kuhl, U.; Stöckmann, H.J. Directed emission from a dielectric microwave billiard with quadrupolar shape. *New J. Phys.* **2006**, *8*, 46. [CrossRef]
13. Bäcker, A.; Ketzmerick, R.; Löck, S.; Robnik, M.; Vidmar, G.; Höhmann, R.; Kuhl, U.; Stöckmann, H.J. Dynamical Tunneling in Mushroom Billiards. *Phys. Rev. Lett.* **2008**, *100*, 174103. [CrossRef]
14. Bittner, S.; Dietz, B.; Günther, U.; Harney, H.L.; Miski-Oglu, M.; Richter, A.; Schäfer, F. PT Symmetry and Spontaneous Symmetry Breaking in a Microwave Billiard. *Phys. Rev. Lett.* **2012**, *108*, 024101. [CrossRef] [PubMed]
15. Song, Y.; Monceaux, Y.; Bittner, S.; Chao, K.; Reynoso de la Cruz, H.M.; Lafargue, C.; Decanini, D.; Dietz, B.; Zyss, J.; Grigis, A.; et al. Möbius Strip Microlasers: A Testbed for Non-Euclidean Photonics. *Phys. Rev. Lett.* **2021**, *127*, 203901. [CrossRef]
16. Schrepfer, J.K.; Chen, S.C.; Liu, M.H.; Richter, K.; Hentschel, M. Dirac fermion optics and directed emission from single- and bilayer graphene cavities. *Phys. Rev. B* **2021**, *104*, 155436. [CrossRef]

17. Cao, H.; Wiersig, J. Dielectric microcavities: Model systems for wave chaos and non-Hermitian physics. *Rev. Mod. Phys.* **2015**, *87*, 61–111. [CrossRef]
18. Schermer, M.; Bittner, S.; Singh, G.; Ulysse, C.; Lebental, M.; Wiersig, J. Unidirectional light emission from low-index polymer microlasers. *Appl. Phys. Lett.* **2015**, *106*, 101107. [CrossRef]
19. Wiersig, J.; Hentschel, M. Combining Directional Light Output and Ultralow Loss in Deformed Microdisks. *Phys. Rev. Lett.* **2008**, *100*, 033901. [CrossRef] [PubMed]
20. Song, Q.; Fang, W.; Liu, B.; Ho, S.T.; Solomon, G.S.; Cao, H. Chaotic microcavity laser with high quality factor and unidirectional output. *Phys. Rev. A* **2009**, *80*, 041807. [CrossRef]
21. Yi, C.H.; Kim, M.W.; Kim, C.M. Lasing characteristics of a Limaçon-shaped microcavity laser. *Appl. Phys. Lett.* **2009**, *95*, 141107. [CrossRef]
22. Shinohara, S.; Hentschel, M.; Wiersig, J.; Sasaki, T.; Harayama, T. Ray-wave correspondence in limaçon-shaped semiconductor microcavities. *Phys. Rev. A* **2009**, *80*, 031801. [CrossRef]
23. Yan, C.; Wang, Q.J.; Diehl, L.; Hentschel, M.; Wiersig, J.; Yu, N.; Pflügl, C.; Capasso, F.; Belkin, M.A.; Edamura, T.; et al. Directional emission and universal far-field behavior from semiconductor lasers with Limaçon-shaped microcavity. *Appl. Phys. Lett.* **2009**, *94*, 251101. [CrossRef]
24. Wang, Q.J.; Yan, C.; Diehl, L.; Hentschel, M.; Wiersig, J.; Yu, N.; Pflügl, C.; Belkin, M.A.; Edamura, T.; Yamanishi, M.; et al. Deformed microcavity quantum cascade lasers with directional emission. *New J. Phys.* **2009**, *11*, 125018. [CrossRef]
25. Albert, F.; Hopfmann, C.; Eberspächer, A.; Arnold, F.; Emmerling, M.; Schneider, C.; Höfling, S.; Forchel, A.; Kamp, M.; Wiersig, J.; et al. Directional whispering gallery mode emission from Limaçon-shaped electrically pumped quantum dot micropillar lasers. *Appl. Phys. Lett.* **2012**, *101*, 021116. [CrossRef]
26. Lee, S.Y.; Ryu, J.W.; Kwon, T.Y.; Rim, S.; Kim, C.M. Scarred resonances and steady probability distribution in a chaotic microcavity. *Phys. Rev. A* **2005**, *72*, 061801. [CrossRef]
27. You, M.; Sakakibara, D.; Makino, K.; Morishita, Y.; Matsumura, K.; Kawashima, Y.; Yoshikawa, M.; Tonosaki, M.; Kanno, K.; Uchida, A.; et al. Universal Single-Mode Lasing in Fully Chaotic Billiard Lasers. *Entropy* **2022**, *24*, 1648. [CrossRef] [PubMed]
28. Michel, C.; Doya, V.; Legrand, O.; Mortessagne, F. Selective amplification of scars in a chaotic optical fiber. *Phys. Rev. Lett.* **2007**, *99*, 224101. [CrossRef]
29. Hentschel, M.; Kwon, T.Y. Designing and understanding directional emission from spiral microlasers. *Opt. Lett.* **2009**, *34*, 163–165. [CrossRef]
30. Oskooi, A.F.; Roundy, D.; Ibanescu, M.; Bermel, P.; Joannopoulos, J.D.; Johnson, S.G. MEEP: A flexible free-software package for electromagnetic simulations by the FDTD method. *Comput. Phys. Commun.* **2010**, *181*, 687–702. [CrossRef]
31. Hentschel, M.; Schomerus, H.; Schubert, R. Husimi functions at dielectric interfaces: Inside-outside duality for optical systems and beyond. *Europhys. Lett.* **2003**, *62*, 636. [CrossRef]
32. Berry, M.V.; Robnik, M. Semiclassical level spacings when regular and chaotic orbits coexist. *J. Phys. A Math. Gen.* **1984**, *17*, 2413. [CrossRef]
33. Prosen, T.; Robnik, M. Semiclassical energy level statistics in the transition region between integrability and chaos: Transition from Brody-like to Berry-Robnik behaviour. *J. Phys. A Math. Gen.* **1994**, *27*, 8059. [CrossRef]
34. Tureci, H.E.; Stone, A.D. Deviation from Snell's law for beams transmitted near the critical angle: Application to microcavity lasers. *Opt. Lett.* **2002**, *27*, 7–9. [CrossRef]
35. Rex, N.B.; Tureci, H.E.; Schwefel, H.G.L.; Chang, R.K.; Stone, A.D. Fresnel filtering in lasing emission from scarred modes of wave-chaotic optical resonators. *Phys. Rev. Lett.* **2002**, *88*, 094102. [CrossRef]
36. Hentschel, M.; Schomerus, H. Fresnel laws at curved dielectric interfaces of microresonators. *Phys. Rev. E* **2002**, *65*, 045603. [CrossRef]
37. Schomerus, H.; Hentschel, M. Correcting Ray Optics at Curved Dielectric Microresonator Interfaces: Phase-Space Unification of Fresnel Filtering and the Goos-Hänchen Shift. *Phys. Rev. Lett.* **2006**, *96*, 243903. [CrossRef] [PubMed]
38. Unterhinninghofen, J.; Wiersig, J.; Hentschel, M. Goos-Hänchen shift and localization of optical modes in deformed microcavities. *Phys. Rev. E* **2008**, *78*, 016201. [CrossRef] [PubMed]
39. Harayama, T.; Shinohara, S. Ray-wave correspondence in chaotic dielectric billiards. *Phys. Rev. E Stat. Nonlinear Soft Matter Phys.* **2015**, *92*, 042916. [CrossRef] [PubMed]
40. Stockschläder, P.; Kreismann, J.; Hentschel, M. Curvature dependence of semiclassical corrections to ray optics: How Goos-Hänchen shift and Fresnel filtering deviate from the planar case result. *EPL* **2014**, *107*, 64001. [CrossRef]
41. Stockschläder, P.; Hentschel, M. Consequences of a wave-correction extended ray dynamics for integrable and chaotic optical microcavities. *J. Opt.* **2017**, *19*, 125603. [CrossRef]
42. Goos, F.; Hänchen, H. Ein neuer und fundamentaler Versuch zur Totalreflexion. *Ann. Phys.* **1947**, *436*, 333–346. [CrossRef]
43. Goos, F.; Lindberg-Hänchen, H. Neumessung des Strahlversetzungseffektes bei Totalreflexion. *Ann. Phys.* **1949**, *440*, 251–252. [CrossRef]